AD_____

Award Number: W81XWH-10-1-0836

TITLE: Challenges of Zinc-Specific Transrectal Fluorescence Tomography to Detect Prostate Cancer

PRINCIPAL INVESTIGATOR: Guan Xu
                                          Daqing Piao Ph.D.

CONTRACTING ORGANIZATION: Oklahoma State University
                                          Stillwater, OK 74078-5031

REPORT DATE: October 2011

TYPE OF REPORT: Annual Summary

PREPARED FOR: U.S. Army Medical Research and Materiel Command
                        Fort Detrick, Maryland 21702-5012

DISTRIBUTION STATEMENT: Approved for Public Release;
                                          Distribution Unlimited

The views, opinions and/or findings contained in this report are those of the author(s) and should not be construed as an official Department of the Army position, policy or decision unless so designated by other documentation.

REPORT DOCUMENTATION PAGE

1. REPORT DATE	2. REPORT TYPE	3. DATES COVERED
October 2011	Annual Summary	15 September 2010 – 14 September 2011

4. TITLE AND SUBTITLE

Challenges of Zinc-Specific Transrectal Fluorescence Tomography to Detect Prostate Cancer

5a. CONTRACT NUMBER

5b. GRANT NUMBER
W81XWH-10-1-0836

5c. PROGRAM ELEMENT NUMBER

6. AUTHOR(S)

Guan Xu
Daqing Piao

E-Mail: daqing.piao@okstate.edu

5d. PROJECT NUMBER

5e. TASK NUMBER

5f. WORK UNIT NUMBER

7. PERFORMING ORGANIZATION NAME(S) AND ADDRESS(ES)

Oklahoma State University
Stillwater, OK 74078-5031

8. PERFORMING ORGANIZATION REPORT NUMBER

9. SPONSORING / MONITORING AGENCY NAME(S) AND ADDRESS(ES)
U.S. Army Medical Research and Materiel Command
Fort Detrick, Maryland 21702-5012

10. SPONSOR/MONITOR'S ACRONYM(S)

11. SPONSOR/MONITOR'S REPORT NUMBER(S)

12. DISTRIBUTION / AVAILABILITY STATEMENT
Approved for Public Release; Distribution Unlimited

13. SUPPLEMENTARY NOTES

14. ABSTRACT

We developed novel instrumentation and algorithm methods in response to the challenges specific to prostate cancer detection by trans-rectal fluorescence tomography imaging of the negative-uptake distribution of zinc-specific fluorophore. Specifically,
• we demonstrated a new configuration of swept-spectral-encoding for sequential-source-excitation in DOT that is applicable to FDOT for rapid differentiation of fluorescence excited by DC sources in the current system;
• we developed a new reconstruction algorithm in DOT that is extendable to FDOT for mitigating the significantly depth-dependent sensitivity in trans-rectal imaging geometry for improving target localization in depth;
• we performed synthetic study on reconstructing "negative-contrast" fluorescence anomaly under spatial-prior, by a two-step region-wise FDOT reconstruction algorithm.

15. SUBJECT TERMS
Prostate cancer, zinc, diffuse optical tomography, fluorescence diffuse optical tomography.

16. SECURITY CLASSIFICATION OF:			17. LIMITATION OF ABSTRACT	18. NUMBER OF PAGES	19a. NAME OF RESPONSIBLE PERSON USAMRMC
a. REPORT	b. ABSTRACT	c. THIS PAGE			19b. TELEPHONE NUMBER *(include area code)*
U	U	U	UU	19	

TABLE OF CONTENTS

1. INTRODUCTION

1.1 Objective
The _long-term objective_ of this research is to device the technology of trans-rectal fluorescence diffuse optical tomography (FDOT) to utilize zinc-specific fluorescent marker for detection of prostate cancer. The _specific aims_ of this research are centered on developing methods to overcome the unique challenge of the proposed technology.

1.2 Background
Zinc is a well-established metabolic marker of prostate cancer [1]. Benign prostate tissues secrete zinc in the form of $Zn_3Citrate_2$, and zinc has a concentration of approximately 10mM in prostatic fluid. In cancerous prostate tissue the zinc secretion ceases, resulting in five to ten folds of reduced level of zinc in the associated prostatic fluid. If a zinc-tagging fluorophore can be administered to the prostate, the concentration distribution of the fluophore will be proportional to that of the free zinc, and the uptake of the zinc-specific fluorophore by cancerous prostatic tissue will be ideally none or practically much less than that by normal or benign prostatic parenchyma, which we call it the "_reverse-uptake_" case. The detection of prostate cancer by use of zinc-specific fluorophore then needs to recover a weak target (or targets) of interest within a strong background fluorescence, which is contrary to the convention of reconstructing a strong target (or targets) of interest within a medium of weak-fluorescence.

1.3 Specific aims
This research has the following aims to achieve: (A) _to study algorithms_ that render FDOT reconstruction of "_reverse-uptake_" target fluorescence in _trans-rectal imaging geometry_; (B) _to develop methods of extracting the spatial information_ from imagery of sagittal trans-rectal ultrasound for prior-guided trans-rectal FDOT reconstruction; (C) _to configure trans-rectal ultrasound-coupled FDOT detection system_ for timely acquisition of fluorescence.

More specifically, trans-rectal FDOT of zinc-specific fluorescence for prostate cancer detection is subjected to the following technological challenges: (1) to reconstruct a fluorescence distribution wherein the target has a "_negative contrast_" with respect to a strong background; (2) to recover a fluorescence distribution in an endo-rectal imaging geometry that poses _significant spatially-variant (depth-dependent) sensitivity_ in the measurement. As the experimental FDOT study is to base upon a continuous-wave system that we developed previously for DOT imaging, an additional challenge to FDOT exists, which is (3) to rapidly _differentiate fluorescence signals excited by multiple steady-state sources_. Besides the above three FDOT challenges, another demanding issue is to export the spatial profile of prostate from 2-dimensional imagery of _sagittal trans-rectal ultrasound (TRUS)_ (versus the conventional imagery of transverse TRUS) for the spatial prior to trans-rectal FDOT. These needs in trans-rectal FDOT of zinc-specific fluorescence provoke non-conventional approaches for system instrumentation and reconstruction algorithm.

1.4 Overview of the key progresses in year 1
During the first 12-months of this study, we developed novel instrumentation and algorithm methods for overcoming the challenges (2) and (3) described above, and studied the challenge (1) described above. _The novel instrumentation approach_ is to utilize a wavelength-swept light source for swept-spectral-encoded, sequential source delivery for rapid DOT that is to be

extended to rapid FDOT measurements. We have also implemented *a new algorithm* of "geometric-differential-sensitivity" framework that is different from the methods previously demonstrated [2-6] for mitigating the spatially-variant sensitivity. This algorithm has been tested on DOT and is being extended to FDOT. As TRUS is to be integrated to FDOT, *region-wise reconstruction of "negative-contrast"* by use of the spatial *prior* assumed from TRUS is also investigated by simulation.

During the first 12-months of this study, the PI has also been trained by taking courses, presenting in conferences, and publishing in journals, for his future academic career.

2. BODY

2.1 Swept-spectral-encoded sequential source excitation for DOT and FDOT

The imaging system for this FDOT research has to capitalize the trans-rectal DOT system we developed that is configured for steady-state (DC) detection of multiple source-detector pairs by a spectrometer and a CCD. Since our system was in DC, there has been two ways to differentiate multiple source-channels for DOT detection as indicated in Fig. 1: (1) a time-multiplexing method by mechanical switching, and (2) a spectral-encoding technique by parallel use of discrete laser sources or by using a narrow-band light source after splitting the light with a grating. The method (1) can be applied to FDOT detection, however, the mechanical switching is limited by the date acquisition the speed; the method (2) can reach rapid data acquisition, however, it cannot be applied directly to FDOT measurement [8-10] because the fluorescence signals excited by simultaneously applied DC source-channels of slightly different wavelengths cannot be differentiated.
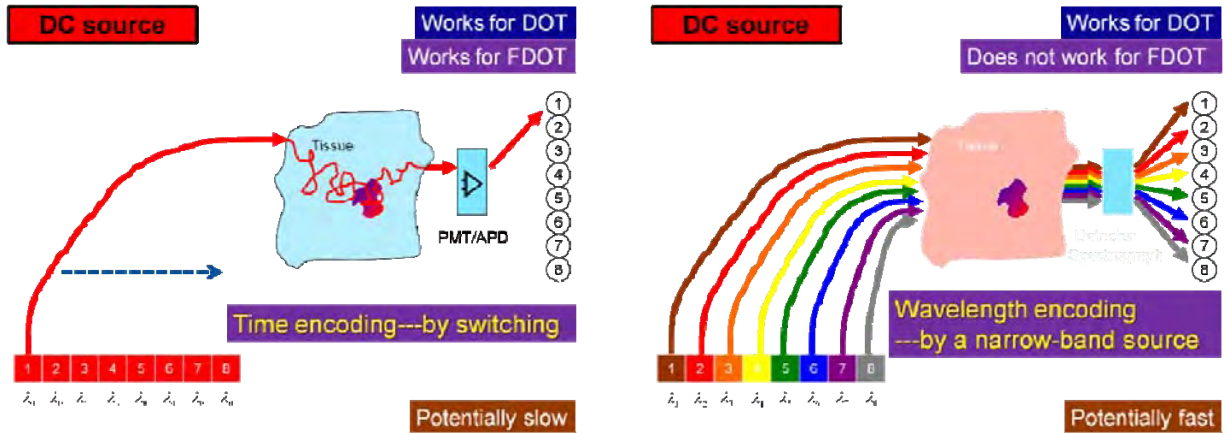

Fig 1. Source-endoding technique. (1) Mechanical swithing works for both DOT and FDOT. (2) wavelength-encoding works for DOT, but not for FDOT.

There are the need of utilizing our existing DOT system for FDOT, and the necessity of rapid FDOT data acquisition in the trans-rectal imaging mode. In this research we have demonstrated a swept-spectral-encoding source-encoding technique that works well for DOT and has the potential of rapid FDOT data acquisition of steady-state fluorescence (steady-state in the sense of neither in frequency-domain nor in time-domain), it can make our current detection unit adaptable to FDOT measurement. The idea is to time-multiplex steady-state sources that excite the fluorescence, by sweeping the wavelengths of the sources in a band of excitation spectrum---

a "swept-spectral-encoding" technique. This technique is an evolution of the spread-spectral-encoding technique we demonstrated for rapid and endoscopic DOT by using a broad-band light source [11-12]. By sweeping the source wavelength, the source channels will be excited sequentially, as shown in Fig. 2, so the fluorescence excited by different "steady-state" source (again, neither being modulated for frequency-domain detection nor short-pulsed for time-domain detection) can be differentiated. This method has the potential of reaching higher acquisition speed than mechanically switching source-channels for steady-state fluorescence detection in the geometry we use for prostate imaging.
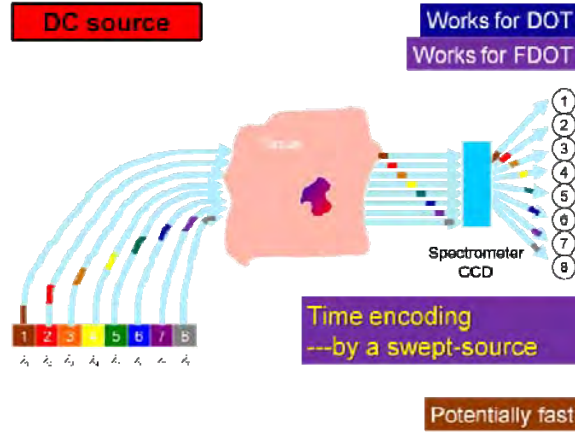

Fig 2. Swept-spectral-endoding of the source allows sequencing the source excitation rapidlly thereby differenting the emission channels rapidly in FDOT mode.

A. System configuration

The swept-spectral-encoding method is first demonstrated in DOT. As is shown in Fig. 3(a), the light from a swept-source is dispersed by a spectrometer (spectrometer #1). The dispersed light beam thereby linearly scans across the exit window of the spectrometer #1 and is sequentially coupled to the source channels linearly arranged at the output plane of the spectrometer #1. At the detection end, the detector signals from each source channel is dispersed by another spectrometer (#2) and focused onto the CCD sensor. The CCD captures one image for each source channel sequentially when a specific channel is illuminated.
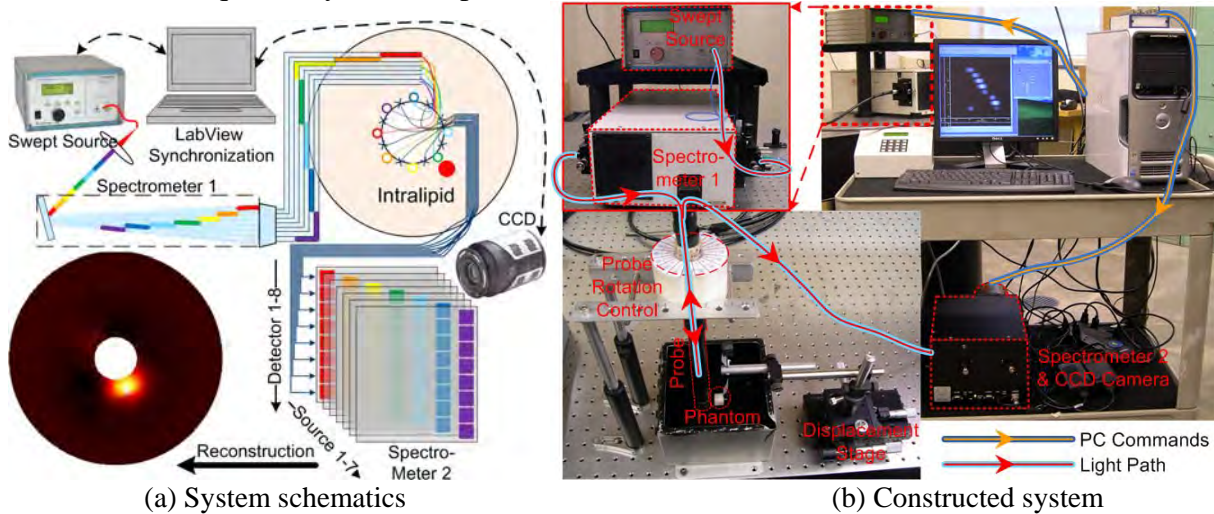

(a) System schematics (b) Constructed system

Fig. 3 System illustration for the swept-spectral-encoding based DOT

Figure 3(b) shows the actual system fabricated. A 4mW Superlum BS-840-02 tunable semiconductor light source is controlled by Labview to sweep in the range of 838nm to 858nm at an increment of 0.05nm. The highest sweeping speed is 100nm/ms. The source light is lead out by a single-mode fiber and collimated by Thorlabs C230TME-B (focal length 4.51mm), producing a 0.08 mm-diameter light beam cross section for coupling to the 1mm diameter source-channel fibers of the DOT applicator. The detection is done by a PIXIS 512 CCD camera with 12.3mm×12.3mm imaging area through a SpectroPro 2300i spectrometer with 300mm focal length. Source-detector synchronization is achieved by National Instruments' DAQ card using LabView. For each imaging cycle, the PC first sends command to tune the source light to the predetermined wavelengths at which maximum light power is coupled. Afterwards, an external trigger signal is send to the CCD camera to capture detection signals. Limited by the source power, a minimum exposure time of 170ms and an extra 150ms CCD readout time is required before tuning the source light to the next source channel. Therefore for each channel, omitting the PC commands transferring time, approximately 320ms is required, which is equivalent to approximately 0.5 per second frame rate. However such acquisition duration can be reduced if the source is more powerful and the CCD has faster data transfer rate.

We used an axial-imaging DOT applicator of 20m in diameter [7] to demonstrate the principle. As is shown in Fig. 4, the 8 source channels and 8 detector channels are fabricated evenly interspersed around the perimeter of the 20mm-diameter probe cross-section. However, one source channel (marked in Fig. 4(d)) is discarded because of its significantly low coupling efficiency due to fabrication defect.
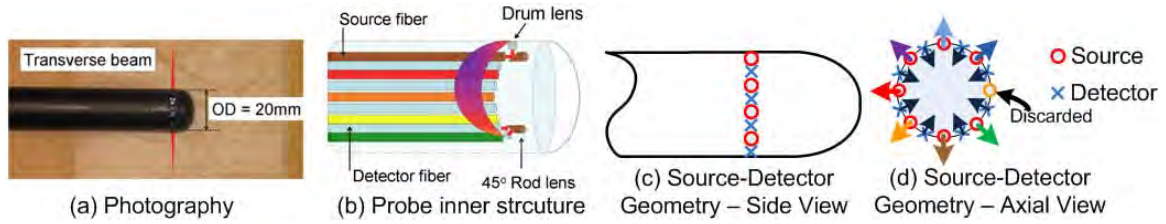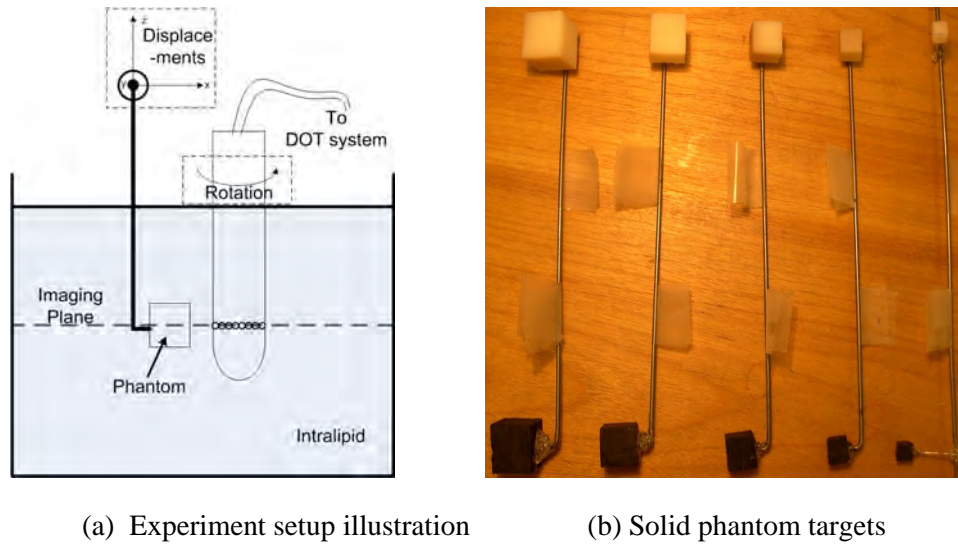

Fig.4 A circular endoscopic imaging geometry

(a) Experiment setup illustration   (b) Solid phantom targets

Fig. 5 Experiment setup and materials

The setup for experimental validation is shown in Fig. 5(a). The probe (applicator) is submerged in a 10"×10"×5" tank filled with intralipid. The inner walls of the tank are painted black to minimize the reflection. The solid phantom targets to be imaged are fabricated with black plastic with assumed infinite absorption contrast to the background intralipid, and material with known optical properties of μ_a= 0.0056 mm^{-1} and μ_s'=1.03 mm^{-1}. As is shown in Fig. 5(b), side lengths of the phantom cube ranges from 5mm to 15 mm. The centers of the targets are placed at the imaging plane of the probe and the horizontal stages are used to control the displacement of the targets. Further, the probe is rotated with respect of the targets to examine the azimuthal sensitivity of the system.

B. Imaging single target of different sizes

The system is first examined by targets with varied sizes as shown in Fig. 6. The side lengths of the target are 5, 7.5, 10, 12.5, and 15mm, respectively. Black plastic materials are reconstructed with obviously higher optical absorption properties as shown in Fig. 6(b) compared to the known-value phantoms as shown in Fig. 6(c). For all five target sizes, the targets made with black plastic are recovered at the same azimuthal location although the recovered volumes decrease with respect to those of the actual targets. For the known-value phantom targets, the absolute absorption values are close to the actual ones when the cubic volume is sufficiently large. However, targets with volumes less than 10×10×10 mm^3 are overwhelmed by background artifacts.
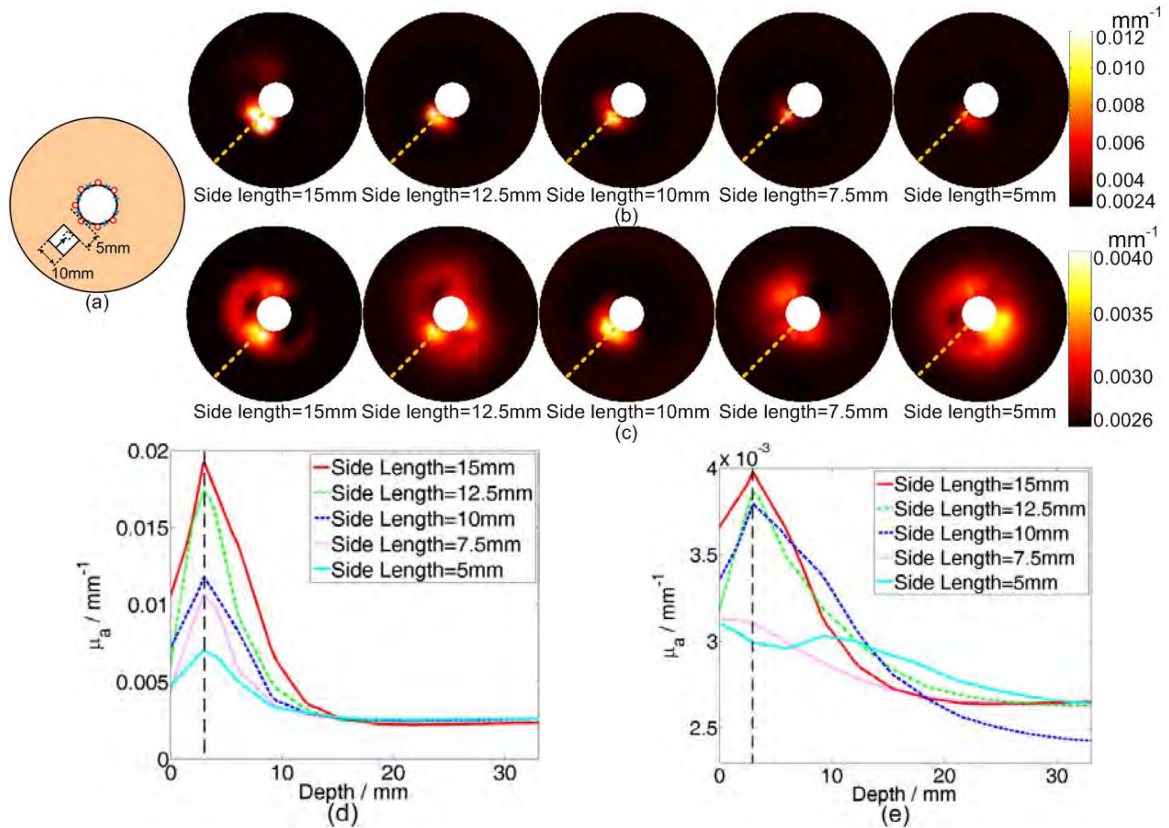

Fig. 6 Experiment on recovering single target of different size. (a) Target location and size illustration; (b) Reconstruction results on black plastic targets; (c) Reconstruction results on known-value phantom targets; (d) Absorption coefficients plotted along the dash lines in (b); (e) Absorption coefficients plotted along the dash lines in (c).

C. Imaging single target at different depths

The system is also examined with targets at varied depth as shown in Fig. 7. A $10\times10\times10$ mm³ cube fabricated from black plastic is imaged at side-to-probe distances from 0mm to 15mm (equivalent center depths of 5mm to 20mm). Recovered absorption distributions are shown in Fig. 7(b) and the absorption values are again plotted along the probe radial direction. It is observed that 1) target deeper than 15mm center-depth is difficult to recover; 2) the recovered volume decrease as the depth increases; and 3) similar to experiment shown in Fig.4, all of the target centers are recovered closer to the probe at the depth of approximately 3mm instead of the actual varied depth up to 15mm. The depth recovery inaccuracy will be discussed later when introducing a new reconstruction algorithm for better target localization in depth.
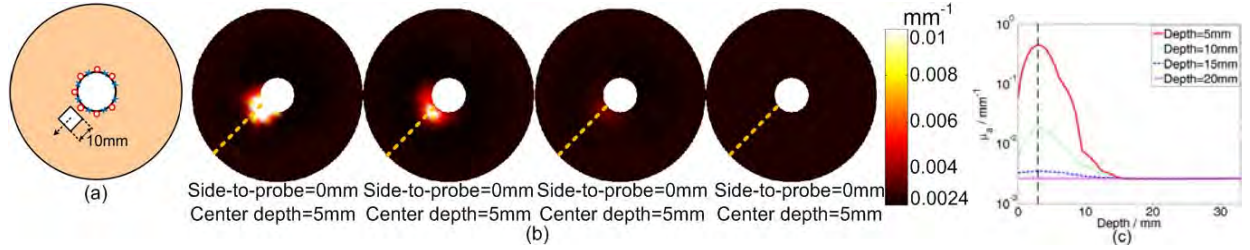

Fig. 7 Experiment on recovering target at different depths. (a) Target location and size (b) Reconstruction results on $10\times10\times10$ mm³ black plastic targets (c) Absorption coefficients plot along the dash lines in (b)

D. Imaging single target at different azimuthal positions

We also examined the azimuthal uniformity by setting a target 3mm away from the optical array at varied angular position as shown in Fig. 8. The target depths are desirably recovered in all positions studied as the target is located at the most sensitive region of the imaging geometry. Absorption values are plotted along the 3mm deep circle off the probe (Fig. 8(c)), as is delineated in Fig. 8(b) by the gold dash lines. Although the values fall into the same order, a maximum of 4 times absolute values difference is observed. The azimuthal non-uniformity is mainly related to imperfection in probe fabrication.
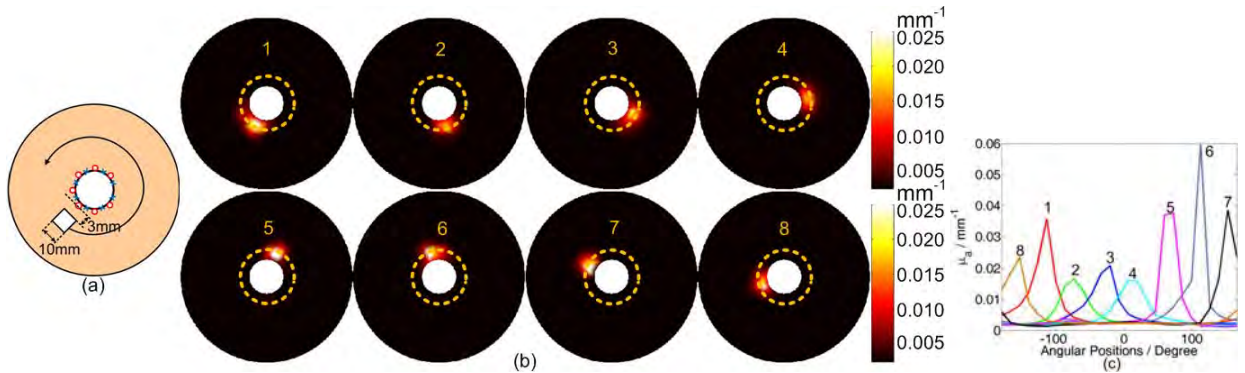

Fig. 8 Experiment on system sensitivity along azimuthal direction (a) Target location and size illustration (b) Reconstruction results (c) Absorption coefficients plot along the dash lines in (b)

We have successfully demonstrated the swept-spectral-encoded sequential source excitation for DOT. By filtering the emission light from the excitation band at detection, the method is readily applicable to FDOT, which is to be demonstrated in the future stages of the project.

2.2 Geometric-differential-sensitivity (GDS) algorithm to improve depth localization in endoscopic imaging geometry

Due to the unique geometry, endoscopic/trans-rectal DOT (and hence trans-rectal FDOT) is subjected to arguably the highest level of sensitivity variation in depth. The sensitivity variance causes miss-location of a target in depth towards the location of highest sensitivity. We have demonstrated a new algorithm of "geometric-differential-sensivity" (GDS) to improve the depth-localization in endoscopic DOT. The method is extendable to FDOT.

A. Principle of GDS for DOT image reconstruction

The principle of this GDS method is illustrated conceptually in Fig. 9, for an axial-translumenal geometry with 8 sources and 8 detectors evenly interspersed along the array-medium interface as shown in (a). In this geometry, the sensitivity to an optical heterogeneity (e.g, of absorption) versus the depth is represented by the dashed curve shown in (b), with a near-boundary maximum followed by nearly-exponential decay in depth. When the image reconstruction is based upon such spatially-variant sensitivity, a target located at a greater depth (hence a smaller sensitivity) is either not to be recovered at all or to be reconstructed incorrectly in a near-boundary location. Alternatively for an optical heterogeneity at a fixed depth, the shown sensitivity profile resembles the sensitivity of a series of detectors along the circumference, with respect to the same source that is azimuthally closest to the heterogeneity of interest. A differentiation between the sensitivities of two neighboring and source-sharing source-detector pairs to the same heterogeneity carries the same information as the non-differentiated sensitivity does, however with the variation over the depth significantly reduced, as is shown by the solid curve in (b).
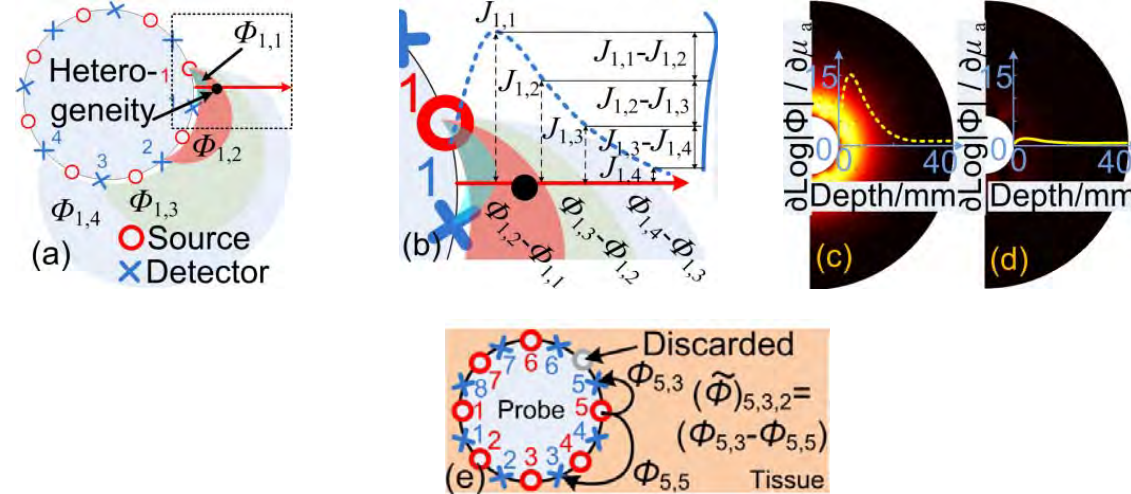

Fig. 9 Conceptual illustration of the principle. (a) Imaging geometry; (b) Magnified area of the dotted box in (a); Depth-dependences of the conventional; (c) and geometric-differential; (d) sensitivity profiles, respectively; (e) Illustration of $\tilde{\Phi}^{\{i,j,k\}}$ in equ. X.

Analytically, the conventional objective function to be minimized during DOT image reconstruction for a pair of source i and detector j, denoted by $\{i, j\}$, can be expressed as

$$\Delta\Psi^{\{i, j\}} = \left\|\Phi_c^{\{i, j\}} - \Phi_m^{\{i, j\}}\right\|^2 = \left\|J_{1\times 2N}^{\{i, j\}} \cdot \delta\mu_{2N\times 1}\right\|^2 \tag{1}$$

where $\Phi_c^{\{i, j\}}$ and $\Phi_m^{\{i, j\}}$ are the calculated and measured photon fluence rates, respectively, $\delta\mu_{2N\times 1}$ is the updates of the optical properties (assuming absorption coefficient μ_a and reduced scattering coefficient μ_s' only) at the total N nodes, and $J_{1\times 2N}^{\{i, j\}}$ is the conventional sensitivity matrix associated with source-detector pair $\{i, j\}$. We now construct a surrogate sensitivity matrix,

$$\tilde{J}_{1\times 2N}^{\{i, j, k\}} = \left(\tilde{J}_{1\times 2N}^{\{i, j\}} - \tilde{J}_{1\times 2N}^{\{i, j+k\}}\right)_{i=1:Nos,\, k=1:Nod-1,\, j=1:Nod-k} \tag{2}$$

where k is the difference between the serial numbers of the detectors, "*Nos*" is the number of source channels, and "*Nod*" is the number of detector channels. We therefore call this method a geometric-differential sensitivity (GDS) approach. The image reconstruction is then to optimize a surrogate objective function [13], as expressed by

$$\Delta\tilde{\Psi}^{\{i, j, k\}} = \left\|\tilde{\Phi}_c^{\{i, j, k\}} - \tilde{\Phi}_m^{\{i, j, k\}}\right\|^2 = \left\|\tilde{J}_{1\times 2N}^{\{i, j, k\}} \cdot \delta\mu_{2N\times 1}\right\|^2 \tag{3}$$

Note that in equ (2) a sign change of the resulted term $\tilde{J}^{\{i, j, k\}}$, represented by $\tilde{J}^{\{i, j, k\}} \Leftarrow -\tilde{J}^{\{i, j, k\}}$, is necessary if $\{k>Nod/2\}$ or $\{k= Nod/2$ & $i<k$ & $j<i\}$ or $\{k= Nod/2$ & $i>k$ & $j+k\geq i\}\}$. The profile of the rearranged surrogate sensitivity $\tilde{J}$, after column-wise summation, is like the one shown in Fig. 9(d) versus the profile of the conventional sensitivity J in Fig.9(c).

A comparison between a conventional sensitivity profile and the GDS profile is illustrated in Fig.9(c) and (d), calculated using NIRFAST [14]. The imaging geometry has an array radius of 10mm and a domain radius of 50mm. The finite element mesh representing the imaging domain includes 7708 evenly distributed nodes and 15040 elements with the Robin-type boundary condition. The dynamic range of the introduced GDS profile over the depth is approximately 1/10 of that of the conventional sensitivity profile over the same depth. The nearly depth-independence of the surrogate sensitivity profile is expected to lead to much improved depth localization when compared to the substantial depth-degradation of the conventional sensitivity profile. However, due to the increase in the matrix size the expected improvement in depth-localization by GDS approach is to be accompanied by an increased demand in computation time.

B. Target localization by GDS-based DOT image reconstruction---single target case
GDS-based endoscopic DOT image reconstruction is examined by simulation and experiments for two sets of targets. The optical parameters employed for the simulation were chosen based on experimental studies. Specifically, the background had μ_a=0.0023 mm^{-1} and μ_s'=1mm^{-1} corresponding to 1% bulk intralipid solution at 840nm. Optical heterogeneity was introduced by use of one or two black-plastic cubes, whose sharp and strong contrast over the background medium was necessary to evaluating the edge-spread-function for depth-localization. The cube-heterogeneity was treated as having μ_a= 0.0115 mm^{-1}, or five times of absorption contrast over the back-ground, and μ_s'= 1.1mm^{-1}. A small scattering contrast was assigned to mitigate the potential cross-coupling between μ_a and μ_s'. A 1% white noise was added to all forward data.

The results are shown in Fig. 10. The array-facing-edge of the cube was located 0, 5, and 10mm away from the optical array, or equivalently with the center depths of 6, 11, and 16 mm, respectively. The results of the conventional and GDS methods on simulated and experimental data are displayed column-wisely, with the actual location of the cube marked with dotted square. In addition, the radial profiles along the green dotted lines crossing the cube location are

compared for each row in logarithmic scale, as is shown in the "Contour Plots". It is observed in simulation that both conventional and GDS methods are capable of recovering targets at depths of 10mm. However, GDS has much better localization of the depth of the target. In the experimental study, the recovering of the target at edge-depths of 0 and 5 mm by the two methods is comparable to that shown by simulations, whereas the GDS has noticeably better depth-localization of the array-facing edge of the cube. At edge-depth of 10mm, neither of the methods could identify the target at the correct location, however, the artifact by GDS method is negligible comparing to that by the conventional method. The contour plots in Fig. 10 imply that in both simulation and experiment, the absorption values recovered by GDS method for different target-depths are all in an interval between e^{-6} to e^{-5}, whereas the absorption values recovered by the conventional method vary in a much greater range. The narrow range of absorption contrast demonstrates an additional aspect of improvements by the GDS method.
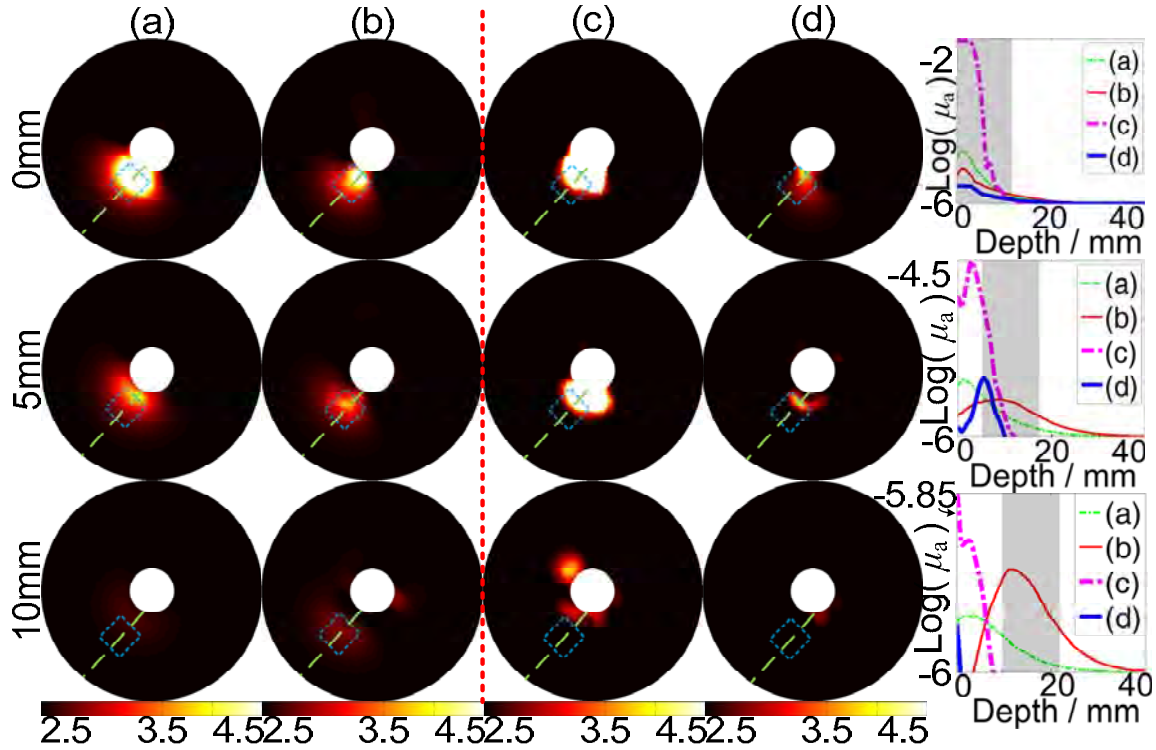

Fig. 10 Simulations and experiments of recoveirng single target (Unit:$10^{-3}\cdot$mm^{-1}). Columns (a) and (b): simulation results by conventional and GDS methods,respectively. Columns (c) and (d): experiement results by conventional and GDS methods, respectively.Blue dotted squares indicate target positions. Contour plots are absorption profiles along the green dotted lines in the reconstruction images. Shaded area in Contour Plots indicates the target locations. GDS improves target depth localiazation and volume estimation.

C. Target differentiation by GDS-based DOT image reconstruction---dual-target case

Figure 11 demonstrates simulation and experimental studies of resolving two black-plastic cubes of 10mm edge-length. The array-facing edges of the cube targets are placed 1mm away from the probe (corresponding to a center depth of 6mm), and the angular separation between the two targets was approximately 90 degrees. The medium conditions and the optical properties assumed for the two cube-targets are the same as those in Fig. 10. The actual target locations are

marked by blue dotted line in Fig. 11(a)-(d). Along the azimuthal cross section of the imaging geometry as is marked with green dotted circles, the recovered absorption coefficient profiles are displayed in Fig. 11(a)-(d), after a normalization to the peak of the extracted profile as plotted in Fig. 11(e). Simulation results indicate that even though both conventional and GDS methods are able to resolve the two targets, GDS method separates the targets more distinctly. The conventional method based on the experimental data failed to discern the targets, yet the GDS method resolves the two targets at the correct locations with good contrast over the background.
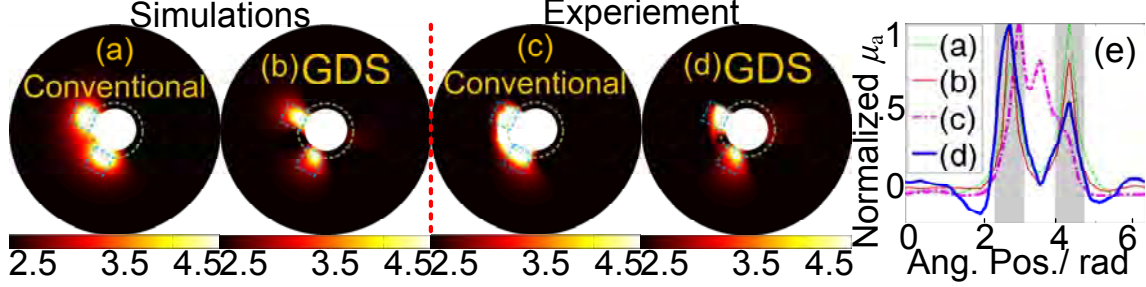

Fig. 11 Simluation and phantom studies on resolving two targets. (Unit:$10^{-3}\cdot mm^{-1}$). (a)-(d) reconstruction images; Blue dotted square indicate the target positions; (e) Absorption contour plotted along the green dotted lines in (a)-(d), shaded area indicating the targets.

D. Prospects of GDS-based FDOT image reconstruction

We have successfully demonstrated a method of mitigating the spatial-variance of sensitivity in endoscopic DOT image reconstruction to improve target localization. We are conducting simulation studies to compare the outcomes of this new algorithm vis-à-vis those of existing methods, such as sensitivity-weighting method. Should this GDS method outperform other existing methods in target localization in depth, it will be applied to endoscopic FDOT, as endoscopic FDOT is subjected to the same level of spatial sensitivity variation as that in endoscopic DOT.

2.3 Synthetic study of "negative-contrast" FDOT with spatial *prior*

Both the instrumentation and computation modeling works in section 1 will be extended to fluorescence imaging. Currently, we have investigated in simulation region-wise FDOT reconstruction of "negative-contrast" targets with assumed spatial prior.

A. Region-wise reconstruction to simultaneously recover emission-band optical properties and the fluorescence yield under spatial prior for negative contrast case

Before presenting the details of our improvement to the region-wise reconstruction algorithm, we review the basis of FDOT reconstruction. Fluorescence optical tomography usually models the propagation of excitation and emission light by

$$\nabla \cdot D_x(\vec{r})\nabla\Phi_x(\vec{r},\omega) + [\mu_{ax}(\vec{r}) + \frac{i\omega}{c}]\Phi_x(\vec{r},\omega) = q_{0,x}(\vec{r},\omega) \tag{4}$$

$$\nabla \cdot D_m(\vec{r})\nabla\Phi_m(\vec{r},\omega) + [\mu_{am}(\vec{r}) + \frac{i\omega}{c}]\Phi_m(\vec{r},\omega) = q_{0,m}(\vec{r},\omega) \tag{5}$$

$$\nabla \cdot D_m(\vec{r})\nabla\Phi_m(\vec{r},\omega) + [\mu_{am}(\vec{r}) + \frac{i\omega}{c}]\Phi_m(\vec{r},\omega) = \Phi_m(\vec{r},\omega)\eta\mu_{af}(\vec{r})\frac{1 - j\omega\tau(\vec{r})}{1 + [\omega\tau(\vec{r})]^2} \tag{6}$$

Where subscript "x" and "m" represents excitation and emission, respectively. Φ is the photon fluence rate. D is the diffusion coefficient and μ_a is the absorption coefficient. $\mu_{af} = \varepsilon_{fl} \cdot c_{fl}$ is the fluorophore absorption coefficient, where ε_{fl} and c_{fl} are the extinction molar coefficient and concentration of the fluorophore, respectively. η and τ are the fluorophore quantum efficiency and life time, respectively. q_0 is the source term. $\vec{r}$ and ω are the pixel position vector and modulation frequency of the source light.

Equations (4) and (5) are usually written together in most literatures, as the differences only existed in the subscripts of "x" or "m". However, more accurate FDOT reconstruction should include the following procedures:

- To implement source light at the excitation band ($q_{0,x}$) and collect diffused light signal at the excitation band (Φ_x at tissue boundaries) and recover absorption and diffusion coefficient distribution (μ_{ax} and D_x) at the excitation band.
- To implement source light at the emission band ($q_{0,m}$) and collect diffused light signal at the emission band (Φ_m at tissue boundaries) and recover absorption and diffusion coefficient distribution (μ_{am} and D_m) at the excitation band.
- To implement source light at the excitation band ($q_{0,x}$) and collect fluorescence emission signal at the emission band (Φ_m at tissue boundaries) and recover fluorescence yield and life time distribution ($\eta\mu_{af}$ and τ) at the excitation band.

Note that the emission band signals in the second step are generated by external source light at the emission band, whereas those in step three are generated by fluorophore. The first two steps can be replace by multi-spectral DOT measurements and reconstruction for more reliable determination of $\mu_{ax,m}$ and $D_{x,m}$ values. However, such arrangement requires external light sources at more wavelengths.

As region-wise reconstruction in FDOT is over-determined at most cases, the unknown parameters in step two (μ_{am}, D_m) can be solved simultaneously with those in step three ($\eta\mu_{af}$ and τ). Such arrangement in image reconstruction actually reduces the complexity of FDOT system, as the external source light at the emission band is no longer necessary. The reconstruction is therefore reduced to two steps:

- Implement source light at the excitation band ($q_{0,x}$) and collect diffused light signal at the excitation band (Φ_x at tissue boundaries) and recover absorption and diffusion coefficient distribution (μ_{ax} and D_x) at the excitation band.
- Implement source light at the excitation band ($q_{0,x}$) and collect fluorescence signal at the emission band (Φ_m at tissue boundaries) and recover absorption/diffusion coefficient distribution (μ_{am} and D_m) and fluorescence yield/life time distribution ($\eta\mu_{af}$ and τ) at the excitation band.

We only utilize DC fluorescence measurements for reconstruction, $\omega=0$ and $\tau=0$ in equ. (4)-(6).The Jacobian structure of the first step is constructed following the conventional method and we structured the sensitivity matrix (Jacobian) in the second step following equ. (4):

$$
\begin{bmatrix}
\dfrac{\partial \ln I_{11}}{\partial \mu_{am}} & \dfrac{\partial \ln I_{11}}{\partial D_m} & \dfrac{\partial \ln I_{11}}{\partial \eta\mu_{af}} & \dfrac{\partial \ln I_{11}}{\partial \tau} \\
\dfrac{\partial \ln I_{12}}{\partial \mu_{am}} & \ddots & \ddots & \vdots \\
\vdots & \ddots & \ddots & \vdots \\
\dfrac{\partial \ln I_{77}}{\partial \mu_{am}} & \cdots & \cdots & \dfrac{\partial \ln I_{77}}{\partial \tau}
\end{bmatrix}
\tag{7}
$$

And the sensitivity matrices are substituted into Levernberg-Marquardt method for iteratively solving the unknown values.

$$x_{k+1} = x_k - [J^T(x_k)J(x_k) + \mu I]^{-1} J^T(x_k) \nu(x_k) \tag{8}$$

The region-based reconstruction is simulated in Fig. 12 for the case of the target haing positive optical contrast over the background but negative-contrast of fluorescence-yield, and in Fig. 13 for the case of the target having negative optical contrast over the background and negative-contrast of fluorescence-yield. The imaging domain is a 80mm×80mm×80mm cube. Substructures are segmented according to the presumed spatial *prior*. The optical array includes 7 sources and 7 detectors, arranged in parallel rows at the bottom of the imaging geometry. The (b)-(f) of Fig. 12 and 13 shows the optical properties assignment of the two cases of medium-target. We assume the optical properties are accurately determined in step one and only the second step is simulated. μ_{ax}=0.006, μ'_{sx}=1. The fluorescence quantum efficiency is set to 0.1 for all regions. The reconstruction initial values are set as: μ_{am} =0.01, μ'_{sm} =1 and $\eta\mu_{af}$ =0.0001. Table.1 and 2 compares the assigned and the reconstructed values of . Note that the scattering coefficients ($\mu'_{sx,m}$ =1/(3· $D_{x,m}$)- $\mu_{ax,m}$) are shown instead of showing $D_{x,m}$.
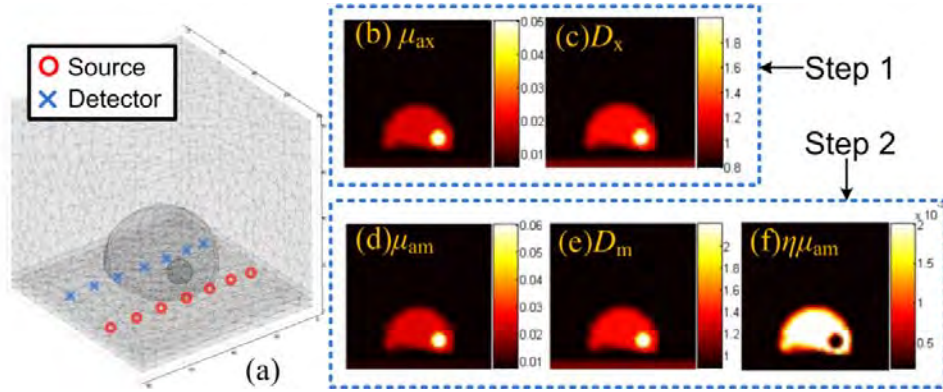

Fig.12 Simulation geometry and procedures with region-wise reconstruction algorithm for positive-optical-contrast and negative-fluorescence-yield. (a) Simulation geometry; (b)-(d) μ_{ax} and μ'_{sx} distribution, reconstruction parameters in the step 1; (d)-(f) μ_{am} /μ'_{sm}/$\eta\mu_{af}$ distribution, reconstruction parameters in the step 2.
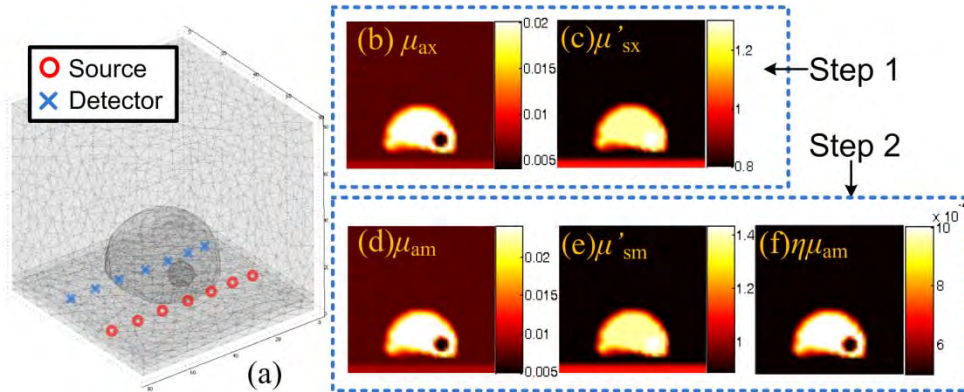

Fig.13 Simulation geometry and procedures with region-wise reconstruction algorithm negative-optical-contrast and negative-fluorescence-yield. (a) Simulation geometry; (b)-(d) μ_{ax} and μ'_{sx} distribution, reconstruction parameters in the step 1; (d)-(f) μ_{am} /μ'_{sm}/$\eta\mu_{af}$ distribution, reconstruction parameters in the step 2.

In Table 1 and 2, although the reconstructed values do not agree exactly with the set values, the relative positive or negative contrasts among the regions are accurately identified.

Table 1 Comparison between the set values and the reconstruction results given in Fig. 12. Note: The optical properties in excitation band is assumed as known, only the unknown parameters in the second step (Fig.10 (d)-(f)) are recovered here.

	regions	μ_{am} / mm^{-1}	μ'_{sm} / mm^{-1}	μ_{am} / mm^{-1}	μ'_{sm} / mm^{-1}	μ_{af} / mm^{-1}
Set values	peripheral tissue	0.006	0.8	0.0072	0.88	0.0018
	prostate	0.02	1.25	0.0240	1.375	0.0200
	rectum	0.008	1	0.0096	1.1	0.0018
	tumor	0.05	2.0	0.06	2.2	0.0018
Reconstructed values	peripheral tissue	-	-	0.0070	0.88	0.0018
	prostate	-	-	0.0240	1.444	0.0194
	rectum	-	-	0.0095	1.104	0.0018
	tumor	-	-	0.04	1.465	0.0015

Table 2 Comparison between the set values and the reconstruction results given in Fig. 13. Note: The optical properties in excitation band is assumed as known, only the unknown parameters in the second step (Fig.10 (d)-(f)) are recovered here.

	regions	μ_{am} / mm^{-1}	μ'_{sm} / mm^{-1}	μ_{am} / mm^{-1}	μ'_{sm} / mm^{-1}	μ_{af} / mm^{-1}
Set values	peripheral tissue	0.006	0.8	0.0072	0.88	0.001
	prostate	0.02	1.25	0.0240	1.375	0.002
	rectum	0.008	1	0.0096	1.1	0.001
	tumor	0.004	1.3	0.0048	1.43	0.001
Reconstructed values	peripheral tissue	-	-	0.0072	0.88	0.001
	prostate	-	-	0.0259	1.23	0.0024
	rectum	-	-	0.0094	1.11	0.0010
	tumor	-	-	0.0027	1.22	0.0020

2.4 Future works

Future works include the following aspects of the study: (1) to demonstrate swept-spectral-encoding sequential source excitation for FDOT data acquisition; (2) to extend GDS method to FDOT reconstruction of both "positive" and "negative-contrast" cases; (3) to configure phantom and experimental setup to study negative-contrast fluorescence detection; (4) to develop method of extracting spatial profile of prostate from 2-dimensional imagery of quasi-sagittal TRUS.

3. KEY RESEARCH ACCOMPLISHMENTS

- Demonstrated a new method of source-encoding in DOT that is extendable to FDOT for rapid differentiation of fluorescence excited by DC sources.
- Developed a new reconstruction algorithm in DOT that is extendable to FDOT for mitigating the significantly depth-dependent sensitivity in trans-rectal imaging geometry.
- Implemented a two-step FDOT reconstruction algorithm to the synthetic study of region-wise reconstruction of "negative-contrast" fluorescence anomaly.

4. REPORTABLE OUTCOMES

The research has lead to the following publications.

Journal and proceeding publications

- Xu G, Piao D, Dehghani H, "The utility of direct-current as compared to frequency domain measurement in spectrally-constrained diffuse optical tomography toward cancer imaging," *Technol Cancer Res Treat*.; 10(5):403-16 (2011).
- Xu G, Piao D, "Feasibility of rapid near-infrared diffuse optical tomography by swept-spectral- encoded sequential light delivery," *Proc. SPIE* 7896, 78961W (2011).
- Xu G, Piao D, Dehghani H, "Spectral a priori to spatial a posteriori in continuous-wave image reconstruction in near-infrared optical tomography," *Proc. SPIE* 7892, 78920D (2011).

Conference abstracts and presentations

- Xu G, Piao D, "Challenges of and new configurations toward fluorescence diffuse optical tomography of zinc-specific biomarker for prostate cancer detection", poster presentation in *2nd Innovative Minds in Prostate Cancer Today (IMPaCT) Conference* for research funded by the Department of Defense (DOD) Prostate Cancer Research Program (PCRP), Mar. 09-11, 2011, Orlando, FL. Paper PC094694-1920.
- Xu G, Piao D, "Near-infrared diffuse optical tomography based on a wavelength-swept light source" *Research Symposium 2011, Oklahoma State University*. The presentation was selected to the First-place of oral presentations in Biomedical Science.

Course works and research compliance training

- The PI has taken courses such as Optical System Design and Laser Spectroscopy offered in Physics department for additional course-work training. He earned grades of A from both courses.

5. CONCLUSIONS

In conclusion, progress in both instrumentation and computational aspects pertinent to trans-rectal FDOT of negative fluorphore uptake have been investigated during the first 12-months of this project. These progresses are related to the tasks specified in the Statement of Work as being summarized in the following:

Task 1: *Synthetic study on FDOT of fluorescence-strong targets within a weak background and FDOT of fluorescence-weak targets within a strong background (partially completed)*
In fulfillment of task one, a region-wise reconstruction algorithm simplifying the measurement procedures in conventional FDOT has been developed and validated by synthetic studies. A geometric-differential-sensitivity reconstruction algorithm for DOT is also derived for the depth-dependent sensitivity distribution in the endoscopic remission imaging geometry. The effectiveness of the algorithm in DOT is confirmed by both computational simulation and

phantom experiments. The effectiveness of the algorithm will be examined in FDOT by simulation and experimental studies.

Task 2: *Optimize image processing techniques to extract spatial prior from TRUS for 3-D FEM model generation (postponed).*
As the instrumentation works in first year focus on the optical part, ultrasound imaging modality is not yet integrated into the system. The proposed work for ultrasound image processing is to be fulfilled along with the completion of the task 3.

Task 3: *Experiment system development and validation (partially completed).*
A system based on swept-spectral-encoding of the source channels is demonstrated for DOT. This novel configuration, with the optical filtering implemented, will allow rapid FDOT of fluorescence excited by multi-channel DC sources. Further studies will be directed toward experimentally demonstrating that targets of negative fluorescence contrast with respect to the background can be recovered, with the investigated instrumentation and algorithm methods..

REFERENCES

1. V. Zaichick, T. Sviridova, and S. Zaichick, "Zinc concentration in human prostatic fluid: Normal, chronic prostatitis, adenoma and cancer," International Urology and Nephrology **28**, 687-694 (1996).
2. B. W. Pogue, T. O. McBride, J. Prewitt, U. L. Österberg, and K. D. Paulsen, "Spatially Variant Regularization Improves Diffuse Optical Tomography," Appl. Opt. **38**, 2950-2961 (1999).
3. J. P. Culver, A. M. Siegel, J. J. Stott, and D. A. Boas, "Volumetric diffuse optical tomography of brain activity," Opt. Lett. **28**, 2061-2063 (2003).
4. M. Huang and Q. Zhu, "Dual-Mesh Optical Tomography Reconstruction Method with a Depth Correction that Uses A Priori Ultrasound Information," Appl. Opt. **43**, 1654-1662 (2004).
5. H. Niu, F. Tian, Z.-J. Lin, and H. Liu, "Development of a compensation algorithm for accurate depth localization in diffuse optical tomography," Opt. Lett. **35**, 429-431 (2010).
6. Q. Zhao, L. Ji, and T. Jiang, "Improving depth resolution of diffuse optical tomography with a layer-based sigmoid adjustment method," Opt. Express **15**, 4018-4029 (2007).
7. D. Piao, H. Xie, C. Musgrove, C. F. Bunting, W. Zhang, G. Zhang, E. B. Domnick-Davidsion, K. E. Bartels, G. R. Holyoak, S. N. Vemulapalli, H. Dehghani, and B. W. Pogue, "Near-infrared optical tomography: endoscopic imaging approach," in (SPIE, 2007), 643103-643110.
8. S. C. Davis, H. Dehghani, J. Wang, S. Jiang, B. W. Pogue, and K. D. Paulsen, "Image-guided diffuse optical fluorescence tomography implemented with Laplacian-type regularization," Opt. Express **15**, 4066-4082 (2007).
9. B. Yuan and Q. Zhu, "Separately reconstructing the structural and functional parameters of a fluorescent inclusion embedded in a turbid medium," Opt. Express **14**, 7172-7187 (2006).
10. J. Lee and E. M. Sevick-Muraca, "Three-dimensional fluorescence enhanced optical tomography using referenced frequency-domain photon migration measurements at emission and excitation wavelengths," J. Opt. Soc. Am. A **19**, 759-771 (2002).

11. D. Piao, S. Jiang, S. Srinivasan, H. Dehghani, and B. W. Pogue, "Video-rate near-infrared optical tomography using spectrally encoded parallel light delivery," Opt. Lett. **30**, 2593-2595 (2005).

12. D. Piao and B. W. Pogue, "Rapid near-infrared diffuse tomography for hemodynamic imaging using a low-coherence wideband light source," Journal of Biomedical Optics **12**, 014016-014012 (2007).

13. K. Lange, D. R. Hunter, and Y. Ilsoon, "Optimization Transfer Using Surrogate Objective Functions," Journal of Computational and Graphical Statistics **9**, 1-20 (2000).

14. H. Dehghani, M. E. Eames, P. K. Yalavarthy, S. C. Davis, S. Srinivasan, C. M. Carpenter, B. W. Pogue, and K. D. Paulsen, "Near infrared optical tomography using NIRFAST: Algorithm for numerical model and image reconstruction," Communications in Numerical Methods in Engineering **25**, 711-732 (2009).

15. Jiang, Z., Piao, D., Holyoak, G. R., Ritchey, J. W., Bartels, K. E., Slobodov, G., Bunting, C. F. & Krasinski, J. S. Trans-rectal Ultrasound-coupled Spectral Optical Tomography of Total Hemoglobin Concentration Enhances Assessment of the Laterality and Progression of a Transmissible Venereal Tumor in Canine Prostate. Urology **77**, 237-242 (2011).